Computers & Structures, Vol. 6, pp. 221–239. Pergamon Press 1976. Printed in Great Britain

BOSOR5—PROGRAM FOR BUCKLING OF ELASTIC-PLASTIC COMPLEX SHELLS OF REVOLUTION INCLUDING LARGE DEFLECTIONS AND CREEP†

DAVID BUSHNELL
Lockheed Missiles & Space Company, Inc., Palo Alto Research Laboratory, Palo Alto, CA 94304, U.S.A.

(*Received* 10 *May* 1975)

Abstract—BOSOR5 can handle segmented and branched shells with discrete ring stiffeners, meridional discontinuities, and multi-material construction. The shell wall can be made up of as many as six layers, each of which is a different nonlinear material. In the prebuckling analysis large-deflection axisymmetric behavior is presumed. Bifurcation buckling loads are computed corresponding to axisymmetric or nonaxisymmetric buckling modes. The strategy for solving the nonlinear prebuckling problem is such that the user obtains reasonably accurate answers even if he uses very large load or time steps. BOSOR5 has been checked by means of numerous runs in which the results have been compared to other analyses and to tests.

The prebuckling and plastic bifurcation (eigenvalue) analyses are described, with the most important equations given. These equations are derived from a finite difference energy method. The strategy for solving problems simultaneously involving large deflections, elastic-plastic material behavior, and primary and secondary creep permits the use of rather large time and load steps without undue sacrifice in accuracy. This strategy is based on a subincremental iteration method in which the size of the subincrement is automatically determined such that the change in stress is less than a certain prescribed percentage of the effective stress. The theoretical treatment of discrete ring stiffeners, the material of which is elastic-plastic and can creep according to a primary or secondary creep law, is also given. Discrete rings of arbitrary cross-section are considered to be assemblages of thin rectangular elements. The structure of the BOSOR5 computer program, which runs on the CDC 6600 and on the UNIVAC 1108 and 1110, is described.

The paper gives comparisons between test and theory for many configurations, including axially compressed cylinders and internally and externally pressurized shells of various shapes with and without ring stiffeners. The results of sensitivity studies are given in which the effect on predicted critical load of various analytical models of the ring-shell wall intersection area are explored. A method of predicting the effect of welding on buckling load is described, and an example involving a ring-stiffened doubly-curved shell is given. Welding the ring stiffeners to a shell introduces residual stresses and geometrical imperfections, both of which reduce the load-carrying capability.

NOMENCLATURE

- $[C]$ Plastic loading matrix, eqns (6) and (25)
- $[D]$ elastic constants defined in eqns (7) and (25)
- ϵ total strain anywhere in the shell wall or discrete ring cross-section
- e_1, e_2 radial, axial distances from ring attachment point to ring centroid
- E elastic modulus
- G shear modulus $= E/[2(1+\nu)]$
- H radial force/length, applied at ring centroid, positive outward (Fig. 3)
- I identity matrix
- $[K]$ integrated constitutive law—eqns (23) and (24) of Ref. [4]
- N, M stress resultants or number of degrees-of-freedom in prebuckling, stability problems
- M Meridional moment about ring centroid, positive clockwise (Fig. 3)
- n number of full circumferential waves in buckling pattern
- p normal pressure
- q dependent variables—nodal displacements and Lagrange multipliers
- δq infinitesimal change in q
- r radius of parallel circle measured to shell reference surface
- R radius of curvature
- s arc length along meridian
- V axial load/length, applied at ring centroid, positive as shown in Fig. 3
- W work done by external forces
- x', y' axial, radial distances measured in ring cross section (Fig. 3)
- z distance from reference surface measured normal to it
- e reference surface strain
- κ reference surface change in curvature
- ν Poisson's ratio
- σ stress
- $\bar{\sigma}$ effective stress, $\bar{\sigma} = (\sigma_1^2 + \sigma_2^2 - \sigma_1\sigma_2)^{1/2}$
- θ circumferential coordinate
- ψ energy gradient or shell wall rotation component, depending on context
- χ meridional rotation

Superscripts

- b infinitesimal buckling quantity
- P plastic
- C creep
- $()'$ $= \mathrm{d}()/\mathrm{d}s$
- $(\dot{})$ $= \mathrm{d}()/\mathrm{d}\theta$
- T thermal; or transpose of matrix, depending on context

Subscripts

- a anywhere in the ring cross-section (Fig. 3)
- b infinitesimal buckling quantity
- c pertains to ring centroid
- $0, o$ prebuckling
- 1 meridional
- 2 circumferential
- 12 shear
- f "fixed" or "not an eigenvalue parameter"
- r pertains to ring
- s pertains to ring shear center
- T tangent modulus
- $()_{,i}$ $\partial()/\partial(\delta q_i)$.
- i pertaining to ith degree of freedom or ith shell element.

†Presented at the Second National Symposium on Computerized Structural Analysis and Design at the School of Engineering and Applied Science, George Washington University, Washington, D.C., 29–31 March 1976.

Symbols
- ⌊⌋ Row vector
- {} Column vector
- [] Matrix

ANALYSIS

1.1 *Axisymmetric prebuckling analysis*

1.1.1 *General equations.* Details of the nonlinear prebuckling analysis are given in[1–3]. Only the main features will be summarized here. The theory is valid for small strains and moderately large rotations. The material behavior is modeled by means of J_2 flow theory with isotropic strain hardening and primary or secondary creep. The creep law incorporated into B0S0R5 is given by

$$\bar{\epsilon}^c = A\bar{\sigma}^m t^n \tag{1}$$

where $\bar{\epsilon}^c$ is the effective creep strain, $\bar{\sigma}$ is the effective stress, and t is the time.

For each of a sequence of time steps a system of N nonlinear equations

$$\psi_i(q_j) = 0 \quad i = 1, 2, \ldots N \qquad j = 1, 2, \ldots N \tag{2}$$

is solved by the Newton–Raphson method. The quantity N is the number of degrees-of-freedom in the discrete model. For each Newton-Raphson iteration the equations

$$\sum_{j=1}^{N} \frac{\partial \psi_i}{\partial q_j} \Delta q_j = -\psi_i \quad i = 1, 2, \ldots N \tag{3}$$

must be solved for the correction terms Δq_j. Iterations continue until $|\Delta q_j/q_j| < 0.001$. In eqns (2) and (3) q_j are the nodal point degrees-of-freedom; ψ_i is the gradient of the energy functional with respect to q_i:

$$\psi_i = \int_v [\sigma] \left\{ \frac{\partial \epsilon}{\partial q_i} \right\} dV - \frac{\partial W}{\partial q_i} \tag{4}$$

and $\partial \psi_i / \partial q_j$ is the (i, j)th element of the tangent stiffness matrix:

$$\frac{\partial \psi_i}{\partial q_j} = \int_v \left([\sigma] \left\{ \frac{\partial^2 \epsilon}{\partial q_i \partial q_j} \right\} + \left[\frac{\partial \epsilon}{\partial q_j} \right] [I - C]^T [D] \left\{ \frac{\partial \epsilon}{\partial q_i} \right\} \right) dV - \frac{\partial^2 W}{\partial q_i \partial q_j}. \tag{5}$$

1.1.2 *Analysis of the shell.* In eqns (4) and (5) ⌊⌋{} indicate row and column vectors consisting in this axisymmetric prebuckling analysis of two stresses (σ_1, σ_2) or strains (ϵ_1, ϵ_2). Subscripts 1 and 2 denote "meridional" and "circumferential." The 2×2 matrix $[C]$ is filled with zeroes if the material is elastic or unloading. If the material is being loaded into the plastic region, $[C]$ is given by

$$[C] = \frac{\left\{ \frac{\partial \bar{\sigma}}{\partial \sigma} \right\} [\partial \bar{\sigma} / \partial \sigma][D]}{H' + [\partial \bar{\sigma} / \partial \sigma][D] \left\{ \frac{\partial \bar{\sigma}}{\partial \sigma} \right\}}. \tag{6}$$

The various parameters in eqn (6) are

$$\bar{\sigma} \equiv [\sigma_1^2 + \sigma_2^2 - \sigma_1 \sigma_2]^{1/2} \quad [D] \equiv \frac{E}{1 - \nu^2} \begin{bmatrix} 1 & \nu \\ \nu & 1 \end{bmatrix} \tag{7}$$
$$H' = EE_T/(E - E_T)$$

where E_T is the tangent modulus. The uniaxial stress-strain curve is modeled as a series of up to 50 straight line segments.

The quantity W in eqns (4) and (5) is the work done by external forces. The stresses σ_1 and σ_2 are given by

$$\{\sigma\} = \lfloor \epsilon - \epsilon^P - \epsilon^C - \epsilon^T \rfloor [D] \tag{8}$$

where superscripts P, C and T denote "plastic", "creep" and "thermal". The total strains ϵ_1, ϵ_2 are given at any point in the shell wall by

$$\epsilon_\alpha = (e_\alpha - z\kappa_\alpha)/(1 + z/R_\alpha) \quad \alpha = 1, 2 \tag{9}$$

where z is the distance from an arbitrarily located reference surface and

$$\begin{aligned} e_1 &= u' + w/R_1 + \chi^2/2 \\ e_2 &= ur'/r + w/R_2 \\ \kappa_1 &= w'' - u'/R_1 - u(1/R_1)' \\ \kappa_2 &= \chi r'/r \\ \chi &= w' - u/R_1 \end{aligned} \tag{10}$$
$$(\,)' \equiv \mathrm{d}(\,)/\mathrm{d}s.$$

The positions of the shell nodal displacements are shown in Fig. 1. Derivatives of the dependent variables u and w are replaced by appropriate first and second order finite difference formulas for variable nodal point spacing. The "u" nodal points are located midway between "w" nodal points, as shown in Fig. 1. Lagrange multipliers are introduced to include constraint conditions. The subscripted variable q in eqns (2) and (3) thus represents "u" and "w" nodal degrees-of-freedom and the Langrange multipliers.

Integration with respect to the circumferential coordinate θ amounts to multiplication by 2π; integration along the meridian is replaced by multiplication by the arc length L between two adjacent "u" nodes; and integration through the shell thickness is accomplished by Simpson's rule. The shell consists of up to 6 layers, each with a minimum of 5 integration points through its thickness, and each with its own stress–strain curve. The entire structure can consist of up to 25 segments branched in an arbitrary

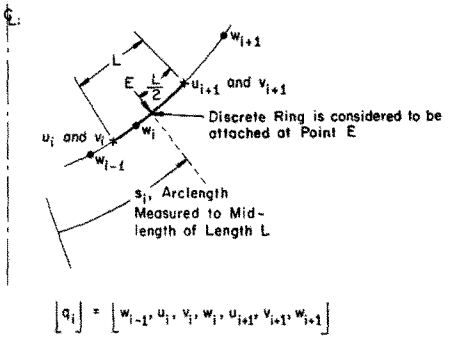

Fig. 1. Locations of shell nodal point variables q_i associated with displacement and rotation of a discrete ring attachment point. The discrete ring energy is ultimately expressed in terms of these variables.

way as long as each segment has the same axis of revolution.

1.1.3 *Analysis of the discrete rings.* In B0S0R5 each discrete elastic–plastic ring is assumed to consist of an arbitrary number of straight segments of uniform thickness as shown in Fig. 2. The material of the rings may creep according to the law given by eqn (1). In the

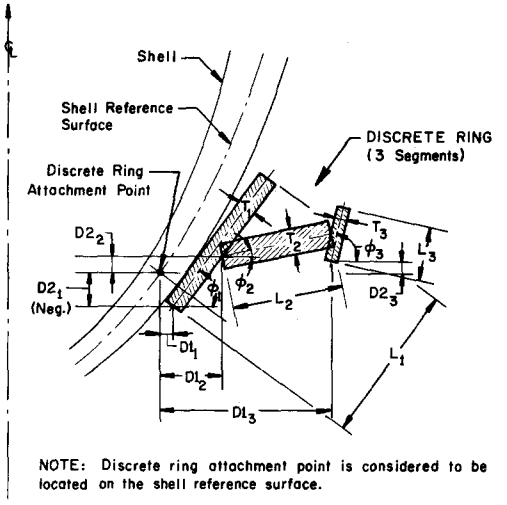

Fig. 2. Discrete ring as modeled in the B0S0R5 computer program.

axisymmetric prebuckling analysis, the hoop strain anywhere in the cross-section of the ring is given by

$$\epsilon_0 = \frac{1}{r_c}\left(1 - \frac{x'}{r_c} + \frac{x'^2}{r_c^2}\right)[A_1 + A_2 x' + A_3 y'] \tag{11}$$

in which

$$\begin{aligned} A_1 &= W_{0s} - y_c\chi_0 + x_c\chi_0^2/2 \\ A_2 &= -\chi_0^2/2 \\ A_3 &= \chi_0. \end{aligned} \tag{12}$$

Subscript $()_0$ denotes "prebuckling." The variables are identified in Fig. 3. The contributions of the discrete ring terms to the prebuckling energy gradient ψ_i and tangent stiffness matrix $[\partial\psi_i/\partial q_j]$ are

$$(\psi_i)_r = 2\pi\left[\int_A \frac{E_r}{r_c}[A][X]\{A^i\}\,dA - \int_A E_r(\epsilon^P + \epsilon^C + \epsilon^T) \times (A_1^i + A_2^i x' + A_3^i y')\,dA - r_c\,[-Vu_{0c}^i + Hw_{0c}^i + M_{\chi 0}^i]\right] \tag{13}$$

and

$$\left(\frac{\partial\psi_i}{\partial q_j}\right)_r = 2\pi\left[\int_A \frac{E_r}{r_c}[A][X]\{A^{ij}\}\,dA - \int_A E_r(\epsilon^P + \epsilon^C + \epsilon^T) \times (A_1^{ij} + A_2^{ij}x' + A_d^{ij}y')\,dA + \int_A \frac{E_T}{r_c}[A^i][X] \times \{A^j\}\,dA + r_c \times [-Ve_2 + He_1]\chi_0^i\chi_0^j\right]. \tag{14}$$

These expressions are derived in [2]. Superscripts $()^i$ and $()^{ij}$ denote differentiations of $()$ with respect to the ith and jth nodal degrees-of-freedom. The matrix $[X]$ is

$$[X] = \begin{bmatrix} \left(1 - \frac{x'}{r_c} + \frac{x'^2}{r_c^2}\right) & \left(x' - \frac{x'^2}{r_c}\right) & \left(y' - \frac{x'y'}{r_c}\right) \\ \left(x' - \frac{x'^2}{r_c}\right) & (x'^2) & (x'y') \\ \left(y' - \frac{x'y'}{r_c}\right) & (x'y') & (y'^2) \end{bmatrix} \tag{15}$$

Derivations of eqns (11)–(15) are given in [2]. These terms are to be added to eqns (4) and (5) for any point on the shell reference surface which corresponds to an attachment point of a discrete ring (see Fig. 1).

1.1.4 *Strategy for solving problems with both large deflections and nonlinear material properties.* The prebuckling iteration strategy is as follows: At each load level or time step there are two nested iteration loops. In the inner loop the set of simultaneous non-linear algebraic eqns (2) with given fixed material properties and plastic and creep strains is solved (see the following paragraph, however.) This is the "Newton–Raphson loop." In the outer loop the strain-dependent material properties (the matrix $[C]$), the plastic strain components ϵ_1^P, ϵ_2^P and the creep strain components ϵ_1^C, ϵ_2^C are calculated. Double

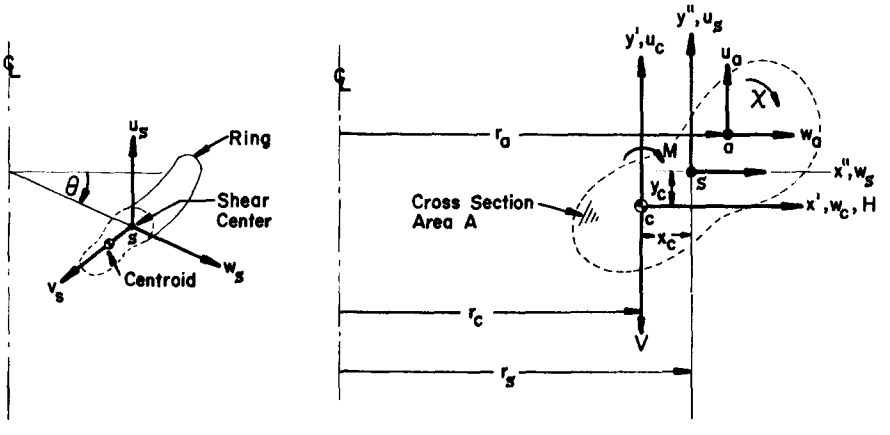

Fig. 3. Discrete ring variables and sign convention.

iterations at a given load level continue until the displacements no longer change. In this way the favorable convergence property of the Newton–Raphson procedure is preserved, equilibrium is satisfied within the degree of approximation inherent in a discrete model, and the flow law of the material is satisfied at every point in the structure.

The description of the iteration strategy is incomplete in[1]. An important point is omitted there. It has to do with how the first term in eqn (5)

$$[\sigma]\left\{\frac{\partial^2\epsilon}{\partial q_i \partial q_j}\right\} = [\epsilon - \epsilon^P - \epsilon^C - \epsilon^T][D]\left\{\frac{\partial^2\epsilon}{\partial q_i \partial q_j}\right\} \quad (16)$$

is treated. Here the plastic strain $\{\epsilon^P\}$ is assumed to be

$$\{\epsilon^P\} = \{\epsilon_0{}^P + \Delta\epsilon^P\} = \{\epsilon_0{}^P + [C](\epsilon - \epsilon_0)\} \quad (17)$$

in which the subscript $()_0$ denotes "value obtained when the material properties were last updated". Thus, within the Newton–Raphson loop, the plastic strain *is* changing, since ϵ, the total strain, is changing in eqn (17) while all other terms therein are constant. However, notice that in this iteration loop there is no test for loading or unloading. Such a test should not be made within the Newton–Raphson loop, but should be applied only for the outer-loop iterations in which the material properties are being updated because a new displacement vector has been calculated. This is an important point and it is regrettable that it is not included in the description of the solution strategy in[1].

1.1.5 *Subincremental method.* A subincremental method for the solution of problems involving large deflections, plasticity, and creep is used in B0S0R5. This method permits the use of large "major" load or time increments. (A "major" increment is one for which the governing equations are repeatedly solved by the Newton–Raphson method until convergence is achieved.) If creep is neglected, the "major" time increment, call it Δt, is subdivided into equal subincrements, dt, such that each effective strain subincrement, $d\bar{\epsilon}$, is less than 0.0002. It is assumed that the total effective strain increment $\Delta\bar{\epsilon}$ is subdivided into $\Delta\bar{\epsilon}/0.0002$ equal subincrements, $d\bar{\epsilon}$. This strategy is also suitable for some cases in which secondary creep occurs. However, the strategy does not work well for primary creep or for cases in which the creep law has a high power on stress. For example, it is not possible to determine the creep-buckling pressure of a titanium shell with a reasonable amount of computer time, since the "major" increments have to be unreasonably small for early times. The strategy fails for early times because there is a relatively large amount of creep, which for reasonable time increments leads to prediction of substantial changes in stress. Unless unreasonably small time increments are used the change in state of the material as a function of time cannot be predicted with requisite accuracy.

The new strategy which has been implemented in the B0S0R5 computer program involves determination of the ith subincrement $dt^{(i)}$ such that the maximum change in effective stress $d\bar{\sigma}_{(i)}$ during each $dt^{(i)}$ is less than a certain fixed percentage of the effective stress, $\bar{\sigma}_{(i-1)}$. In B0S0R5 the criterion is

$$d\bar{\sigma}_{(i)}/\bar{\sigma}_{(i-1)} \leq 0.01. \quad (18)$$

This strategy leads to subincrements of varying duration within the "major" increment Δt. The modification of the original strategy as set forth in[1] is described in detail in[3]. A very complete description of the flow of calculations with numerical examples is given in[1] and[3]. Enough information is given in those papers to permit one to set up without too much difficulty a similar strategy applicable to other types of structures. Included in[1] are comparisons between flow theory and deformation theory, comparisons with test results, and charts showing how many iterations and how much computer time are required for solution of the nonlinear equations for several load or time increments.

1.2 *Bifurcation buckling analysis*

1.2.1 *General equations.* If q_0 represents an equilibrium state then $\psi_i(q_0) = 0$, $i = 1, 2 \ldots M$. (The number of degrees-of-freedom M in the stability analysis is more than the number of degrees-of-freedom N in the axisymmetric prebuckling analysis because nonsymmetric buckling modes are permitted). At the bifurcation load there exists a nontrivial infinitesimal displacement distribution δq, henceforth called the buckling mode, such that

$$\psi_i(q_0 + \delta q) = 0, \quad i = 1, 2, \ldots M. \quad (19)$$

The ψ can be expanded in Taylor series about q_0, thus:

$$\psi_i(q_0 + \delta q) = \psi_i(q_0) + \sum_{j=1}^{M}\left(\frac{\partial\psi_i}{\partial(\delta q_j)}\right)_{\delta q \to 0}\delta q_j + \cdots = 0; \quad i = 1,2,\ldots M \quad (20)$$

Since $\psi_i(q_0) = 0$ it follows that

$$\sum_{j=1}^{M}\left(\frac{\partial\psi_i}{\partial(\delta q_j)}\right)_{\delta q \to 0}\delta q_j = 0; \quad i = 1, 2, \ldots M. \quad (21)$$

The criterion for the existence of a non-trivial vector δq is that the determinant of the $M \times M$ matrix $[\partial\psi/\partial(\delta q)]$, evaluated in the limit as $\partial q \to 0$, vanish.

1.2.2 *Analysis of the shell.* The (i, j)th element of the stability matrix $[\partial\psi_i/\partial(\delta q_j)]_{\delta q \to 0}$ can be derived with use of eqn (5) as a starting point. The stress and strain vectors $[\sigma]$, $[\epsilon]$ will now contain three elements rather than two, since the buckling mode may be nonsymmetric:

$$[\sigma] \equiv [\sigma_1, \sigma_2, \sigma_{12}]$$
$$[\epsilon] \equiv [\epsilon_1, \epsilon_2, \epsilon_{12}] \quad (22)$$

in which subscript $()_{12}$ denotes shear. The material property matrix $[I - C]^T[D]$ must include shear stiffness elements not present in the axisymmetric prebuckling analysis. In accordance with the discussion in[4] of cruciform column buckling, the effective shear modulus $\bar{G}$ predicted by deformation theory

$$\bar{G} = 0.5E/(1 + \nu + g) \quad (23)$$

in which

$$g = 3(E/E_s - 1)/2 \quad (24)$$

is used if the material is loading plastically. The quantity E_s is the secant modulus determined from the uniaxial stress-strain curve and regarded as a function of effective strain for biaxial stress. Of course, g is set equal to zero if the material has not yielded or is unloading. In eqn (5) $[I]$ is

the 3×3 identity matrix and $[C]$ and $[D]$ are given by

$$[C] = [0] \text{ if unloading or elastic}$$

$$[C] = \begin{bmatrix} c_{11} & c_{12} & 0 \\ c_{21} & c_{22} & 0 \\ 0 & 0 & 0 \end{bmatrix} \text{ if loading plastically} \quad (25)$$

$$[D] = \frac{E}{1-\nu^2}\begin{bmatrix} 1 & \nu & 0 \\ \nu & 1 & 0 \\ 0 & 0 & \dfrac{(1-\nu^2)}{2(1+\nu+g)} \end{bmatrix}.$$

The elements $c_{11}, c_{12}, c_{21}, c_{22}$ of $[C]$ are given by eqn (6).

The strains ϵ_1, ϵ_2 and ϵ_{12} correspond to the total deformations-finite prebuckling u_0, w_0 plus infinitesimal buckling δu, δv, δw. The meridional and circumferential strains vary through the shell wall thickness according to eqn (9) and the shear strain varies according to

$$\epsilon_{12} = (e_{12} + 2z\kappa_{12})/[(1+z/R_1)(1+z/R_2)]^{1/2}. \quad (26)$$

The volume element dV is

$$dV = r(1+z/R_1)(1+z/R_2)\,dz\,d\theta\,ds. \quad (27)$$

The reference surface strains e and changes in curvature κ in terms of the total displacements u, v, w are:

$$\begin{aligned} e_1 &= u' + w/R_1 + \frac{1}{2}(\chi^2+\gamma^2) \\ e_2 &= \dot{v}/r + ur'/r + w/R_2 + \frac{1}{2}(\psi^2+\gamma^2) \\ e_{12} &= \dot{u}/r + r(v/r)' + \chi\psi \\ \kappa_1 &= \chi' \\ \kappa_2 &= \dot{\psi}/r + r'\chi/r \\ \kappa_{12} &= 2(-\dot{\chi}/r + r'\psi/r + v'/R_2) \end{aligned} \quad (28)$$

in which

$$\begin{aligned} u &= u_0 + \delta u & \chi &= w' - u/R_1 \\ v &= v_0 + \delta v \ (v_0 = 0 \text{ in this analysis}) & \psi &= \dot{w}/r - v/R_2 \\ w &= w_0 + \delta w & \gamma &= \frac{1}{2}(u/r - v' - vr'/r). \end{aligned} \quad (29)$$

Primes indicate differentiation with respect to the meridional arc length s and dots indicate differentiation with respect to the circumferential coordinate θ. It is shown in[4] that the stiffness matrix of the ith shell element can be written in the form

$$\begin{aligned} [H]_i = \pi r_i L_i \{&[B_1 + \chi_{0f}B_2]^T [K][B_1 + \chi_{0f}B_2] \\ &+ [R]^T [N_{0f}][R] + [U]^T [P_f][U] + \lambda\{[R]^T [N_0][R] \\ &+ [U]^T [P][U]\} \\ &+ \lambda\chi_0\{[B_1]^T [K][B_2] + [B_2]^T [K][B_1]\} \\ &+ \lambda^2\chi_0^2 [B_2]^T [K][B_2]\}_i. \end{aligned} \quad (30)$$

Subscript i denotes evaluated at the point "E" of the ith finite difference element (Fig. 1). f denotes "fixed" or "not an eigenvalue parameter", and λ is the eigenvalue parameter. The finite difference element is that portion of the shell designated as being of length L in Fig. 1. A complete derivation of eqn (30) is given in[4]. The quantity r_i is the radius of a latitude at the point "E"; L is the arc length of the finite difference element; $[B_1]$ and $[B_2]$ are 6×7 matrices representing the kinematic relations for the shell reference surface as deformed (χ_{0f}) by the "fixed" portion of the loading; $[K]$ is a 6×6 matrix containing the integrated constitutive equation coefficients, including the effects of prebuckling plasticity; $[R]$ is a 3×7 matrix representing the rotation-nodal displacement relations; $[N_{0f}]$ represents the "fixed" portion of the prebuckling in-plane stress resultants; $[U]$ is a 3×7 matrix representing the relationship between the displacements u, v, w at "E" and the nodal point displacements; and $[P_f]$ represents the "pressure-rotation" effect due to the "fixed" portion of the pressure. During a time increment the deformations and loads change from the "fixed" values χ_{0f}, N_{0f}, P_f to total values $\chi_{0f}+\chi_0$, $N_{0f}+N_0$, P_f+P. The increments, χ_0, N_0, P give rise to the terms in eqn (30) multiplied by λ and λ^2.

1.2.3 *Analysis of a discrete ring attached to the shell.* The details of the derivation of the discrete ring bifurcation buckling equations are given in[2]. The incremental hoop strain in the discrete ring during infinitesimal buckling is

$$\epsilon^b = \frac{1}{r_c + x'}[\dot{v}_{ba} + w_{ba} + \frac{1}{2(r_c+x')}\{\dot{u}_{ba}^2 + (\dot{w}_{ba} - v_{ba})^2\}] \quad (31)$$

where subscript $()_b$ denotes "buckling modal displacement", subscript $()_a$ means "anywhere in the ring cross-section", and $(\dot{})$ indicates differentiation with respect to the circumferential coordinate θ. The (i,j)th element of the incremental stiffness and load-geometric matrices governing stability are derived from

$$\frac{\partial\psi_i^b}{\partial q_j^b} = \int_\theta \int_A \left(\sigma_0 \frac{\partial^2\epsilon^b}{\partial q_i^b \partial q_j^b} + E_T \frac{\partial\epsilon^b}{\partial q_i^b}\frac{\partial\epsilon^b}{\partial q_j^b}\right)(r_c + x')\,dA\,d\theta \quad (32)$$

where σ_0 is the prebuckling hoop stress distribution in the ring cross-section and A is the area of the ring cross-section. There is an additional contribution due to twist. For discrete rings with open, thin cross-sections,

$$\left(\frac{\partial\psi_i^b}{\partial q_j^b}\right)_{\text{twist}} = \int_\theta \left[\frac{1}{3}\int_s \bar{G}t^3\,ds\right] r_c\kappa_{xy,i}\kappa_{xy,j}\,d\theta \quad (33)$$

where t is the section thickness which may vary with the distance s measured along the ring cross-section. In eqn (33) $\bar{G}$ is the elastic-plastic shear modulus given by eqn (23) and κ_{xy} is the twist. Subscripts $()_{,i}$ and $()_{,j}$ denote differentiation with respect to the i_{th} and j_{th} nodal point displacement components. More details are given in[2]. These discrete ring contributions are added to the local stiffness matrix $[H_i]$ for the shell if the ith element contains a discrete ring attachment point.

The global stiffness matrix is calculated by appropriate superposition of the local 7×7 matrices $[H_i]$, $i = 1, 2, \ldots I$, where I is the total number of finite difference elements in the structure. Boundary conditions and juncture conditions for compatibility between shell segments are handled by the introduction of Lagrange multipliers.

1.2.4 *Strategy used in B0S0R5 to find minimum bifurcation buckling loads.* The B0S0R5 user chooses a range of circumferential wave numbers, $n_{\min}$ to $n_{\max}$, and a

starting wave number n_0. He also chooses appropriate quasi-static functions of time for the loading. (Distributed loads, line loads, and temperature may all vary differently with time.) The user chooses a time range and time increments such that whatever load range and load increments he is interested in will result. For example, if the user wants to determine the buckling pressure of a shell with some spatial temperature distribution which does not change with time, he provides two time functions for the loading: a constant for the temperature function and a time-linearly-varying pressure coefficient. The actual temperature and pressure are products of the appropriate time functions and spatial distributions. This strategy is essential for problems involving creep and not difficult to get used to in other problems.

Given this input B0S0R5 calculates the determinant of the global stability matrix which consists of terms derived from the first three terms of eqn (30) plus analogous terms contributed by the discrete rings. This determinant is calculated for each time increment until it changes sign or until the specified time range is covered. During this phase of the calculations the circumferential wave number is held constant at n_0.

If the determinant changes sign B0S0R5 sets up, for values of n within the specified range $n_{\min}$ to $n_{\max}$, eigenvalue problems of the type

$$[K_{1n} + \lambda K_{2n}]\{q\} = 0. \tag{34}$$

The quantity $[K_{1n}]$ represents the stiffness matrix corresponding to n circumferential waves for the structure as loaded at the time step just before the determinant corresponding to $n = n_0$ changes sign; $[K_{2n}]$ is the load-geometric matrix derived from the terms

$$[R]^T[N_0][R] + [U]^T[P][U] \tag{35}$$

plus analogous discrete ring terms. In expression (35), N_0 and P represent the increments of prebuckling stress resultants and pressure from the time step just before the determinant sign change to the next time step.

The elements containing χ_0 and χ_0^2 appearing in eqn (30) are omitted because many trial cases demonstrated that these terms often give rise to complex eigenvalues which interfere with the inverse power iteration scheme unless especially allowed for. With use of the strategy just described these terms are unnecessary because,

(1) We are not interested in the actual magnitude of the eigenvalues here as much as we are in finding minimum λ_n with varying number of circumferential waves, n. The actual magnitudes of λ_n cannot generally be used to obtain the buckling load, that is

$$N_{cr} \neq N_{0f} + \lambda_n N_0 \tag{36}$$

because the constitutive equation coefficients $[K]$ may change precipituously with increasing load in the neighborhood of the buckling load.

(2) The effect of prebuckling rotations χ_{0f} is included in the first line of eqn (30) and thus is included in the stability stiffness matrix $[K_{1n}]$. If the load increments are of a reasonable magnitude, the effect of prebuckling shape change on the predicted bifurcation buckling load is therefore accounted for in a reasonably accurate manner.

1.2.5 *"Consistent" loading model: a further justification.* In the derivation of the stiffness matrix it has been assumed that the constitutive equation coefficients $[K]$ are independent of the infinitesimal buckling displacements δq. This assumption is in accordance with the "total" or "consistent" loading principle enunciated by Shanley[5], Hutchinson[6] and others. "Consistent" loading means that if the material at a point in the shell is loading plastically before bifurcation, it will also do so in the transition δq to the buckled configuration. If the material is elastic before bifurcation, it will remain so during incipient buckling. In the introduction of[4] are quoted passages from the work of Shanley[5] and Hutchinson[6] which defend the consistent loading model. The following physical argument[4] is presented here to further justify it.

Let us hypothesize that the eigenvalue obtained from the consistent loading model is physically meaningless because a *finite* amount of material which has been loading into the plastic region suddenly unloads in the *infinitesimal* transition from the unbuckled state q to the buckled configuration $q + \delta q$. The effect would be to produce a stiffer structure and hence, in the presence of a given prebuckling state, a higher eigenvalue than would result from the consistent loading model. Suppose also that an eigenvalue and corresponding kinematically admissible mode have been determined from the consistent loading model. Now assume that a new nonlinear equilibrium analysis is performed for the shell with an infinitesimal imperfection of the same shape as this buckling mode. Since the imperfection is infinitesimal the load-deflection behavior will differ from that of the perfect shell only infinitesimally for loads smaller than the lowest eigenvalue obtained from the consistent loading model. If, as hypothesized, this eigenvalue were physically meaningless and the true bifurcation point lies a finite load increment above it, then the material of the infinitesimally imperfect shell would continue to load consistently right through the neighborhood of the bifurcation load calculated by means of the consistent loading model. A contradiction therefore exists: It has just been hypothesized that the eigenvalue from the consistent loading model is physically meaningless because *infinitesimal* perturbations of the form of the buckling mode cause a *finite* amount of the material to unload suddenly. However, the material of an actual shell containing such a perturbation in geometry loads consistently at the eigenvalue calculated from the consistent loading model. Therefore, this eigenvalue must be physically meaningful and must correspond to a bifurcation point on the load-deflection curve of the perfect shell.

2. ORGANIZATION OF THE B0S0R5 PROGRAM

B0S0R5 is actually three programs—a pre-processor, a main-processor and a post-processor. Each of these processors is overlayed. Overlay charts and very brief descriptions of each of the subroutines are given in the Appendix. Figure 4 shows the input data sequence for the pre-processor. The main-processor and post-processor require very few data cards. Any case can be restarted. The program requires approximately 65K decimal words on the UNIVAC 1108 or 1110 and 150 K octal words on the CDC 6600. Typical run times for cases with less than 100 nodal points are less than 5 min. The UNIVAC version performs most calculations in double precision. B0S0R5 can be obtained from the author.

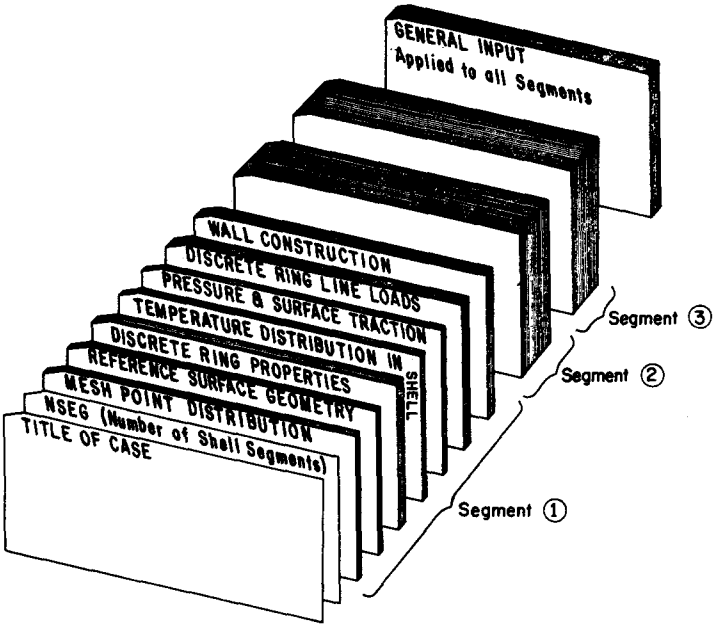

Fig. 4. B0S0R5 pre-processor input deck.

3. NUMERICAL RESULTS

3.1 *General*

The nonlinear elastic–plastic prebuckling analysis of B0S0R5 was checked out through comparisons with experimental and analytical results obtained by Levine *et al.*[7] for a circular flat plate under a centrally applied concentrated load, and with analytical results obtained by Stricklin *et al.*[8] for an internally pressurized torispherical shell. The creep theory and its implementation were checked through comparison with a test reported by Samuelson in[9]. Predicted critical pressures corresponding to axisymmetric bifurcation buckling of a perfect sphere agreed with those obtained by Hutchinson[10] for both flow theory and deformation theory.

3.2 *Axially compressed elastic-plastic cylinders*

Lee[11] and Batterman[12] have tested cylinders under controlled end displacement. Comparisons between these tests and B0S0R5 predictions are given in Tables 1 and 2. In the B0S0R5 analysis the end load was specified rather than the end displacement. The cylinders were assumed to be clamped. If the Batterman cylinders No. 9 and No. 10 (Table 2) are assumed to be simply-supported, the predicted critical axial stresses are reduced to 38,000 and 39,500 psi, respectively.

3.3 *Complex pressurized shells of revolution*

During the past two years Galletly *et al.* at the University of Liverpool have been performing tests on shells of revolution of various shapes under external and internal pressure. The method of testing and some B0S0R5 predictions are given in[13]. These and additional predictions are presented in Figs. 5–12 and Tables 3–5.

For the externally pressurized cone-cylinder shells shown in Fig. 5 the prebuckling plastic flow is confined to narrow axisymmetric bands including the junctures. Accordingly, the B0S0R5 model is set up as shown in Fig. 6, with the plasticity analysis described in[1] being performed only in segments 2 and 3 in order to save computer time. Figure 7 gives the nonsymmetric bifurcation buckling pressures, mode shapes, and critical numbers of circumferential waves. In this case, the effect of plasticity is to produce a hinge at the juncture. (In an elastic analysis of these configurations the hinge would be introduced

Table 1. Comparison of test and theory for axially compressed cylinders

Model	r/t	Test (Lee [1962]) Load (lb)	BØSØR5 Prediction[a]	Highest Test / BØSØR5	Lowest Test / BØSØR5
A300	46.1	5400	5202	1.038	—
A110		9090	8923	1.019	0.884
A210	29.2	8680			
A310		7890			
A120		14500			
A220	19.4	14840	14328	1.036	1.005
A320		14400			
A130		35000			
A230	9.4	36100	33200	1.087	1.054
A330		36000			

[a]Axisymmetric collapse predicted in all cases

Table 2. Comparison of test and theory for axially compressed cylinders tested by Batterman[1965]

Model	r/t	Test Stress (psi)	BØSØR5 Prediction (Clamped Edges)	Test / BØSØR5
9	116.61	31770	44643	.712
8	114.56	33030		
10	113.60	35600	43478	.820
17	89.33	43950		
26	85.95	43690	45063	.970
16	56.52	51380	52282	.983
25	54.93	50640		
15	44.69	55490		
24	44.19	53380	55663	.959
4	26.61	58200		
3	26.56	58200		
2	26.44	57100		
1	26.18	58600		
5	25.94	59570		
6	25.88	58760	57422	1.023
14	19.71	61580	59175	1.041
23	19.66	61480		
13	14.02	64110		
22	13.93	63790	62886	1.014
18	9.76	70000		
19	9.76	69320		
20	9.76	69840	71225	980
12	9.70	69630		
27	9.70	69230		

[a] Axisymmetric collapse predicted in all cases

only in the stability equations, not in the prebuckling equations.)

For the externally pressurized torispherical shells pierced by cylindrical nozzles, an example of which is shown in Fig. 8, a large amount of prebuckling plastic flow is confined to a narrow axisymmetric band including the juncture between the cylindrical nozzle and spherical head. Some plastic flow also occurs near the juncture between the spherical and toroidal portions. Figure 9 shows the B0S0R5 model and predicted prebuckling deflected shape (exaggerated). The critical bifurcation pressures and mode shapes are given in Fig. 10. Tilting of the nozzle was also observed in the tests.

More details of these tests and analysis are given in[13].

The most recent tests by Galletly *et al.* involve internally pressurized torispherical heads made of mild steel and aluminum. Figure 11(a) shows the geometry and location of the nodal points in the B0S0R5 models. Plastic flow prior to buckling occurs in a fairly broad axisymmetric band near the juncture between the spherical and toroidal portions. The thicknesses of the test specimens varied in both the circumferential and meridional directions. B0S0R5 runs were made using the minimum thicknesses measured at each meridional station. These are listed in Table 3. The stress–strain data for the two materials are given in Table 4. Comparisons between tests and theory appear in Table 5; a typical predicted prebuckling deflected shape (exaggerated) is shown in Fig. 11(b); and predicted buckling mode shapes with critical numbers of circumferential waves are given in Fig. 12. Small ranges for the predicted critical buckling pressures are listed in Table 5 because it is known only that for the critical number or range of circumferential waves, the stability determinant changes sign between the minimum and maximum pressures.

A definite explanation of the extreme disagreement between test and theory for the mild steel specimens does not yet exist. It is possible that the buckling mode associated with the lowest predicted eigenvalue grows very little in the post-buckling regime and so this mode was not observed in the tests. Possibly the use of minimum thickness everywhere explains the discrepancy, for this minimum does not actually correspond to any one meridian. However, it is felt that this is not a likely explanation because thicknesses along the local critical meridional arc did have approximately the values given at some point around the circumference.

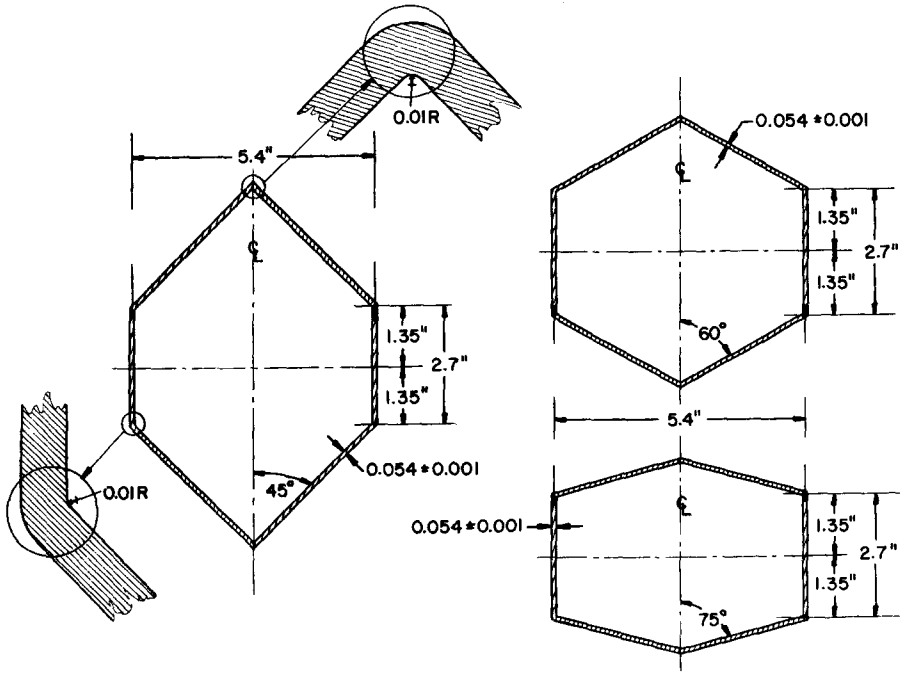

Fig. 5. Aluminum Cone-cylinder specimens tested under external pressure by Galletly at the University of Liverpool.

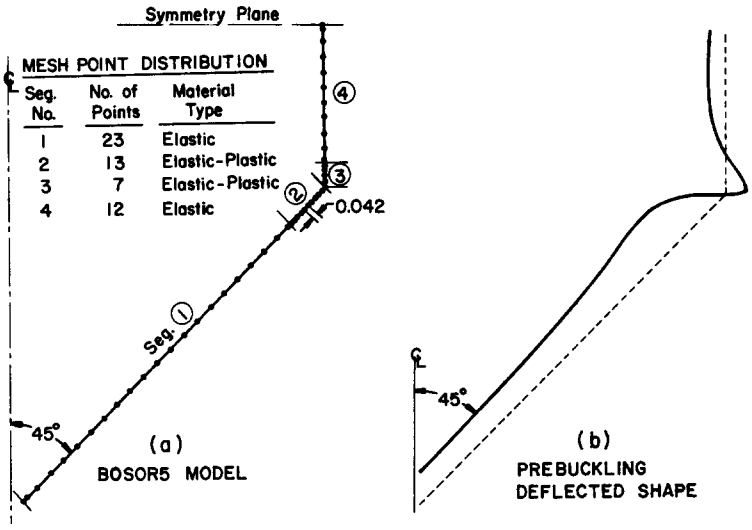

Fig. 6. Discrete Model of the 45° cone-cylinder specimen and exaggerated view of the prebuckling deflected shape at the buckling pressure.

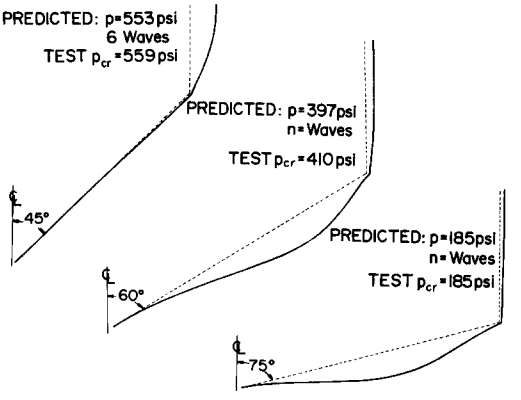

Fig. 7. Bifurcation buckling modes and comparison with test results.

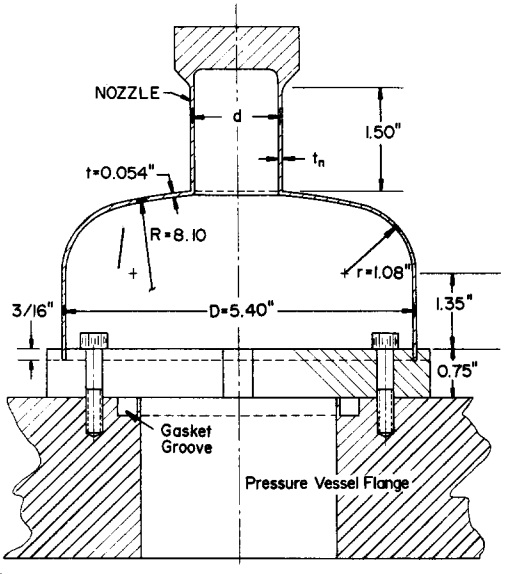

Fig. 8. Aluminum Torispherical head with axisymmetric nozzle tested under external pressure by Galletly at the University of Liverpool.

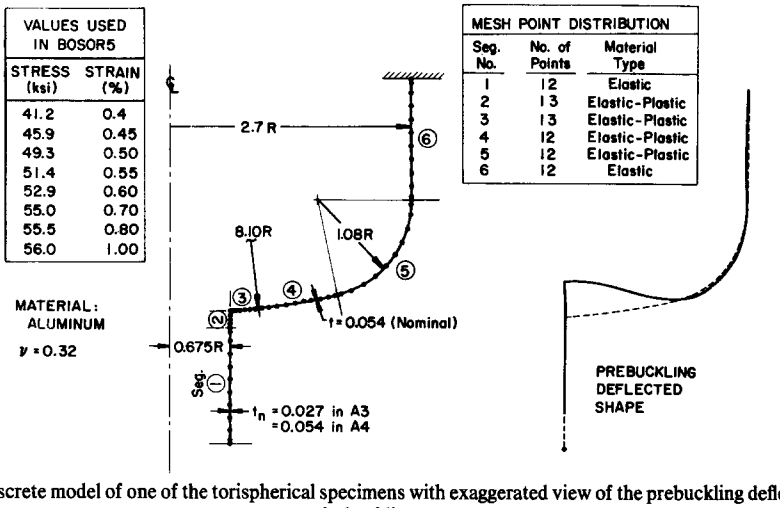

Fig. 9. Discrete model of one of the torispherical specimens with exaggerated view of the prebuckling deflected shape at the buckling pressure.

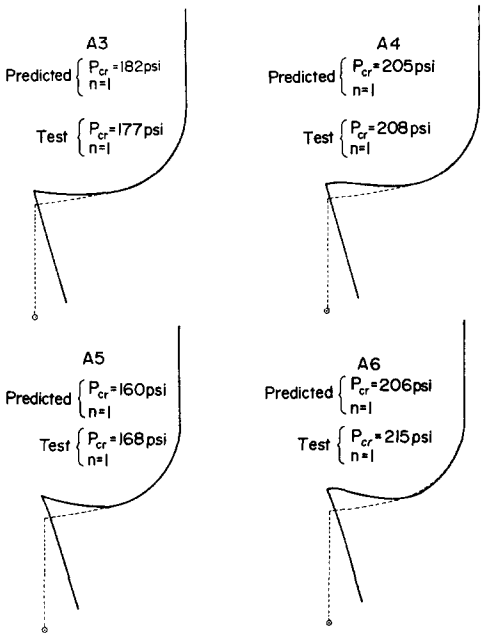

Fig. 10. Bifurcation buckling modes and comparison with test results.

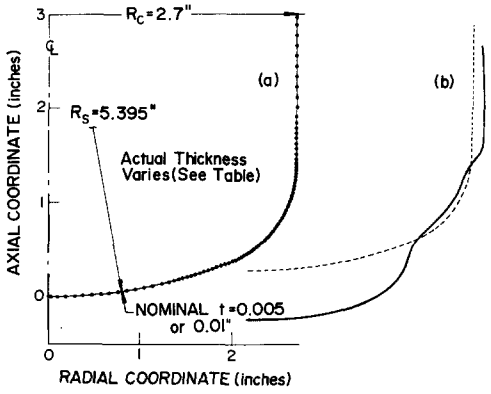

Fig. 11. Aluminum or mild steel torispherical head tested under internal pressure by Galletly at the University of Liverpool: (a) Discrete model, (b) exaggerated view of prebuckling deflected shape at the bifurcation bucklong pressure.

An analysis was conducted to determine the circumferential wave numbers which correspond to critical pressures that agree with the tests. The results are listed in Table 5. The corresponding predicted mode shapes have maxima more toward the cylindrical portion than the mode shapes shown in the top two frames of Fig. 12. Whether or not these findings agree with the tests is not known at this time because the writer was not supplied with information on test mode shapes and critical circumferential wave numbers for the mild steel specimens.

The strategy for finding the critical number of circumferential waves, described in Section 1.2.4, did not work very well for some of these internally pressurized torispherical shells. Bifurcation buckling is caused by the hoop compression which occurs in the region of the knuckle. This hoop compression increases (in absolute value) with pressure initially, but reaches a maximum absolute value and then starts to decrease and even to become tensile as the head flows plastically and becomes more spherical in shape. Some of the specimens buckle nonsymmetrically at pressures for which the absolute value of the hoop compressive stress resultant is decreasing with increasing pressure. For these cases the eigenvalues calculated as described in Section 1.2.4 will have the opposite sign from that expected. However, this does not prevent a determination of the critical bifurcation pressure. It does made the search procedures more onerous.

3.4 *Ring-stiffened cylinders under external hydrostatic pressure*

In[14] are given comparisons between test and theory for 69 machined ring-stiffened aluminum cylinders tested by Boichot and Reynolds[15]. The geometry is given in Fig. 13. Dimensions of all the specimens are tabulated in[14].

Of the 69 test specimens, 24 (designated "*F*", in Fig. 13) had fillets near the boundaries and where the rings join the shell wall. From the photographs in[15], it appears that practically all of the specimens without fillets fractured during failure. However, it is not possible to determine from the test data alone whether fracture caused the failure or whether fracture occurred later as the shell was deforming in its buckling mode. On the other hand, there is almost no evidence of fracture occurring in the case of the 24 specimens with fillets. Therefore, it is reasonable to predict that better agreement between test and theory will

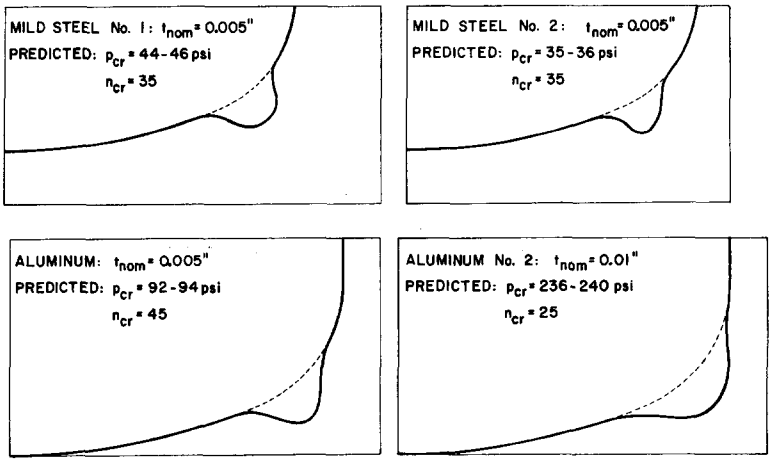

Fig. 12. Bifurcation buckling modes for 4 of the internally pressurized torispherical specimens.

Table 3. Internally pressurized torispherical shells thickness vs axial distance from apex used in the B0S0R5 analysis

	ALUMINUM SPECIMENS						MILD STEEL SPECIMENS			
	t_{nom} = 0.005"		t_{nom} =0.01" SPEC #1		t_{nom} = 0.01" SPEC #2		t_{nom} = 0.005" SPEC #1		t_{nom} = 0.005" SPEC #2	
	(axial distance z in inches, thickness t in mils)									
	z	t	z	t	z	t	z	t	z	t
SEGMENT 1 SPHERICAL	0.0	6.3	0.0	10.4	0.0	10.7	0.0	4.8	0.0	4.6
	0.13	6.3	0.143	10.4	0.13	10.7	0.20	4.8	0.063	4.6
	0.31	5.8	0.33	9.7	0.31	10.5			0.25	3.9
									0.312	3.5
									0.375	3.0
	0.388	5.5	0.388	9.1	0.388	10.5	0.388	5.4	0.388	3.0
SEGMENT 2 TOROIDAL KNUCKLE	0.44	5.5	0.455	8.3	0.56	10.7	0.51	5.0	0.437	3.2
	0.56	6.0	0.517	8.8	0.75	10.3	0.63	3.7	0.500	3.9
	0.75	5.5	0.580	10.2	0.89	10.0	0.82	5.5	0.594	5.1
	0.89	5.4	0.674	10.9	1.16	10.0	0.96	5.5	0.688	5.8
	1.16	5.2	0.768	11.1			1.23	4.7	0.875	6.0
			0.955	10.8					1.094	5.4
			1.174	10.3					1.312	5.0
	1.409	3.8	1.409	10.2	1.409	10.0	1.409	3.6	1.409	5.2
SEGMENT 3 CYLINDRICAL	1.690	4.8	1.705	9.8	1.690	10.6	1.760	5.4	1.625	5.6
	2.06	5.7	2.080	10.2	2.06	10.6	2.130	5.4	2.000	5.5
									2.750	5.6
	3.009	7.2	3.009	10.2	3.009	10.2	3.009	6.0	3.009	5.6

Table 4. Stress-strain data used for the B0S0R5 analysis of the internally pressurized torispherical heads

ALUMINUM SPECIMENS stress (psi)	strain (%)	MILD STEEL SPECIMENS Stress (psi)	Strain (%)
0	0.00	0	0.000
41200	0.40	35400	0.118
45000	0.45	36000	1.300
48150	0.50	38000	1.500
50600	0.55	40000	1.800
52100	0.60		
52750	0.65		
53000	0.70		
54000	0.90		
54000	1.00		

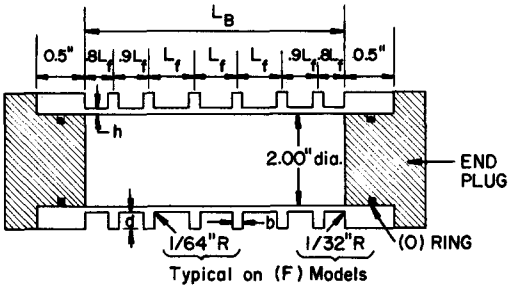

Fig. 13. Aluminum ring-stiffened cylinder tested under external pressure by Boichot and Reynolds at the Naval Ship Research and Development Center, Maryland.

Table 5. Buckling pressures of internally pressurized torispherical heads tested by Gerard Galletly at the University of Liverpool

Material	Specimen	Test Buckling Pressure (psi)	Predicted Buckling Pressure (psi)	Predicted Circumferential Wave Number, n
Mild Steel	.005 #1	127	44 - 46	30 - 40
Mild Steel	.005 #2	78	35 - 36	30 - 38[a]
Aluminum	.005	85	92 - 94	45
Aluminum	.01 #1	215	220 - 226	21
Aluminum	.01 #2	225	236 - 240	25

[a]For n = 21 waves the predicted buckling pressure is in the range 79 to 81 psi.

be obtained for the specimens with fillets than for those without. Furthermore, analytical predictions that are too high for the specimens without fillets would lead one to favor the hypothesis that failure was caused by fracture rather than buckling in these tests, since the analytical model is incapable of predicting fracture. This would be particularly true if the too high predictions correspond to the thicker specimens for which imperfections are less significant.

There are three different nominal radius/thickness ratios involved in the test series: $R/H \cong 12$, 20, and 50. Buckling pressures for the $R/t \cong 50$ specimens are somewhat sensitive to imperfections because buckling, especially of the models in this class with small ring stiffeners, occurs at average stresses that are barely in the plastic range. Indeed the test results for the thinnest specimens exhibit the most scatter, as indicated in Fig. 14.

Figure 14 gives the comparison between test and theory. The generally upward sloping trend results primarily from the fact that the analytical model becomes

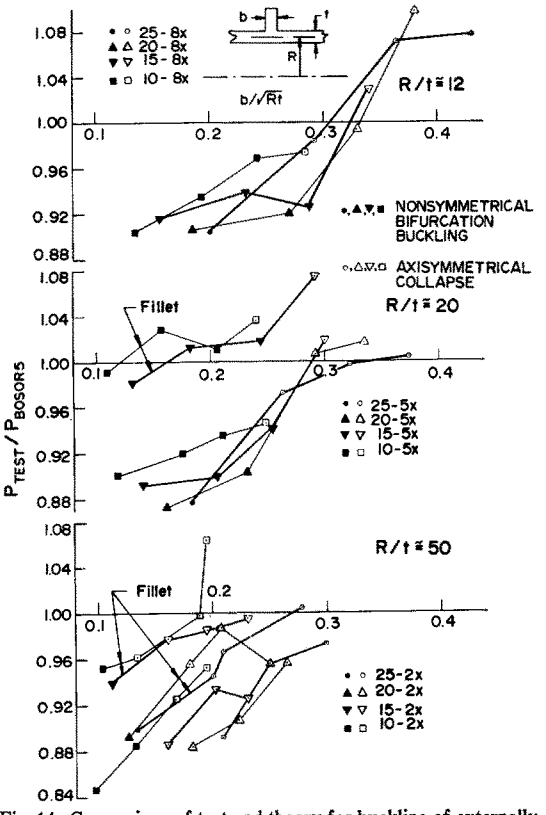

Fig. 14. Comparison of test and theory for buckling of externally pressurized ring-stiffened cylinders plotted as function of ring thickness parameter $b/\sqrt{(Rt)}$.

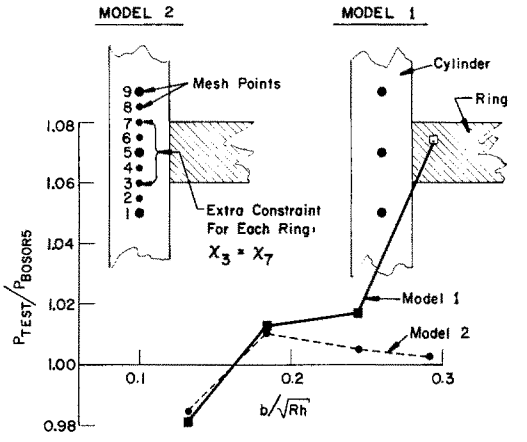

Fig. 15. Comparison of test and theory for specimens 15-5XF neglecting and including ring thickness effect.

increasingly conservative with increasing $b/\sqrt{(Rt)}$: The discrete rings are assumed to be attached to the shell at a single point with the shell free to bend in the axial direction in the immediate neighborhood of this point. The neglected effect on the shell meridional bending stiffness of the finite thicknesses of the rings leads often to predictions of axisymmetric collapse with relatively short axial wavelengths when the test specimens actually fail nonsymmetrically. The short-wavelength axisymmetric mode of failure is hindered by the increased local meridional bending stiffness afforded by the finite axial intersection lengths of shell and rings more than is the relatively long wavelength general instability mode of failure.

With use of B0S0R5, it is possible to investigate analytically the effect on predicted critical pressures of including some additional axial bending stiffness due to the finite axial length of the shell-ring intersection areas. This increase in axial bending rigidity is modeled as shown in Fig. 15. Additional mesh points are provided in the neighborhoods of the discrete rings with meridional rotation constrained to be equal at nodal points corresponding to the bottom and top surfaces of each discrete ring. The solid line, labeled Model 1, corresponds to the original analytical models of the test series 15-5XF in which the discrete ring is considered to be attached at one point and the shell is free to bend under the ring. That is, the prebuckling meridional rotation χ_0 is free to change along the shell wall within the shell-ring intersection area. With the extra constraint conditions (Model 2) the analytical predictions are closer to the test results. The critical failure mode for the specimen with the thickest rings, Specimen 15–58F for which $b/\sqrt{(Rt)} \cong 0.3$, is predicted to be axisymmetric inter-ring collapse with use of Model 1 and nonaxisymmetric general instability with use of Model 2. In the cases for which general nonaxisymmetric instability is predicted with use of Model 1, introduction of extra constraint conditions as depicted in Fig. 15 does not change the prediction very much. Analytical results for all of the cases investigated with use of Model 2 are given in Table 7 of[14]. Unfortunately, the budget for computer time did not permit analysis of the entire series of tests with use of Model 2.

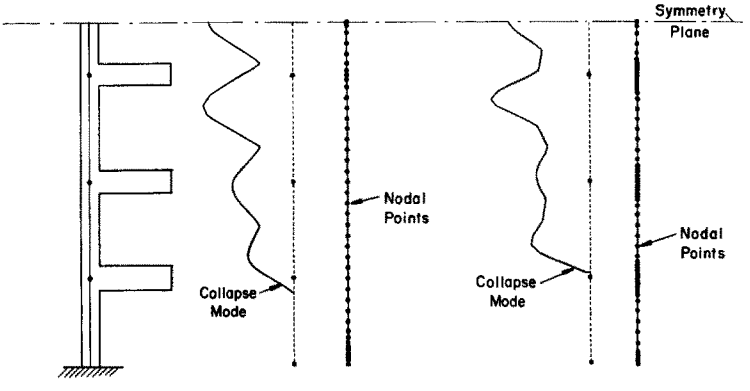

Fig. 16. Predicted axisymmetric collapse model of specimen 25–88: (a) specimen geometry, (b) neglecting ring thickness effect and (c) including ring thickness effect.

Figure 16 shows the predicted axisymmetric failure modes for Specimen 25–88 ($b/\sqrt{(Rt)} = 0.431$) with use of Model 1 and Model 2 analysis. It is clear from these plots why introduction of the extra constraint conditions raises the axisymmetric collapse load.

3.5 *Effect of welding on the buckling pressure of an ellipsoidal ring-stiffened shell*

The geometry of an ellipsoidal shell with internal ring stiffeners is shown in Fig. 17. The purpose of the analysis of this structure is to determine the effect on predicted buckling pressure of axisymmetric distortions and residual stresses due to welding the rings to the shell.

Figure 18 shows the B0S0R5 model, which consists of 313 degrees-of-freedom in the axisymmetric prebuckling analysis and 466 degrees-of-freedom in the nonaxisymmetric stability analysis. Symmetry conditions were imposed at the equator in both the pre-buckling and bifurcation buckling analyses. (It was determined in preliminary runs on the computer that the lowest bifurcation buckling pressure corresponds to a mode symmetric rather than antisymmetric about the symmetry plane.) The locations of the discrete ring attachment points and centroids are indicated in Fig. 18. Table 6 gives the stress–strain curves used in the B0S0R5 analysis.

The effect of the welds shown in Fig. 19(a) is introduced into the analytical model by means of the temperature distribution shown in Fig. 19(b): A certain amount of the material of ring web and shell wall in the neighborhood of the welds is considered to be cooled down below room temperature. The value 1000°F corresponds approximately to the anneal temperature of the steel from which the structure is presumed to be fabricated. The anneal temperature is used as a reference value because residual stresses are relieved for higher temperatures than this. The zero-stress temperature distribution corresponds to the weld region being hot (above 1000°F) and the rest of the material being at room temperature. As the weld material cools down from 1000°F to room temperature, stresses build up in the shell and ring, tensile in the region that was originally heated above 1000°F and compressive elsewhere. Thus, the non-zero stress state corresponds to a uniform ambient temperature distribution. In B0S0R5 it is not possible to generate a nonzero initial thermal stress state with a uniform temperature distribution. Therefore, one must simulate the growth of residual stresses and

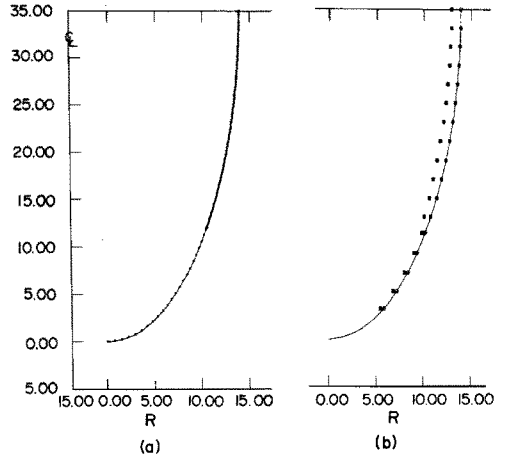

Fig. 18. B0S0R5 model of the ring-stiffened ellipsoidal shell: (a) nodal points, (b) locations of discrete ring attachment points and centroids.

Table 6. Stress–strain curves used in the B0S0R5 analysis of the ellipsoidal shell and stiffeners

	Stress (psi)	Strain (%)
Stiffeners	0.0	0.0
	163000.	.5472
	163000.	10.0
Shell Wall	140000.	.7400
	144560.	.5200
	149450.	.6000
	151400.	.7200
	155300.	1.0200
	157260.	1.6000

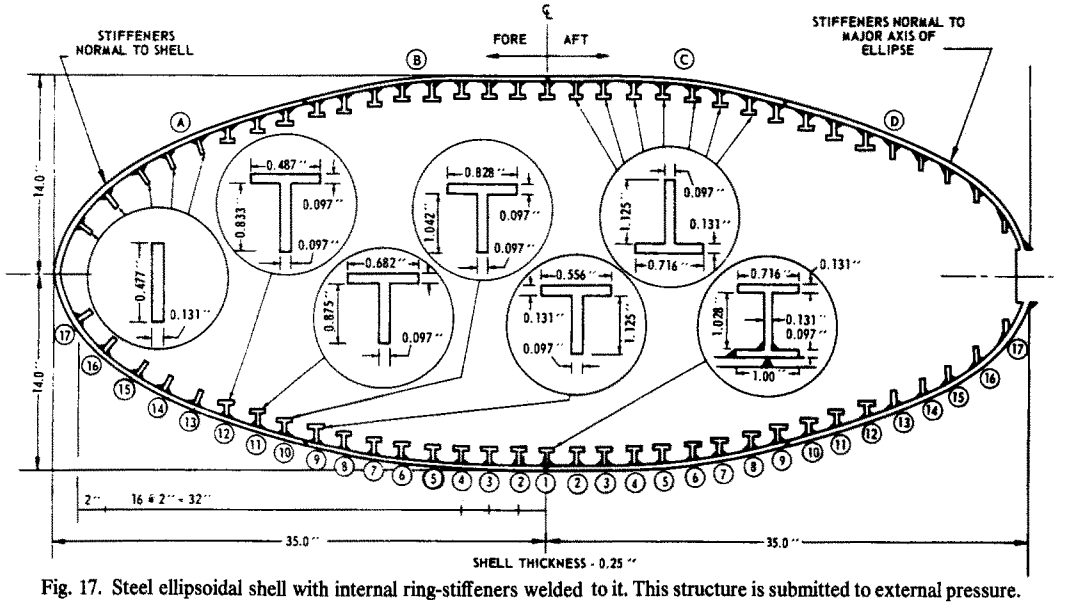

Fig. 17. Steel ellipsoidal shell with internal ring-stiffeners welded to it. This structure is submitted to external pressure.

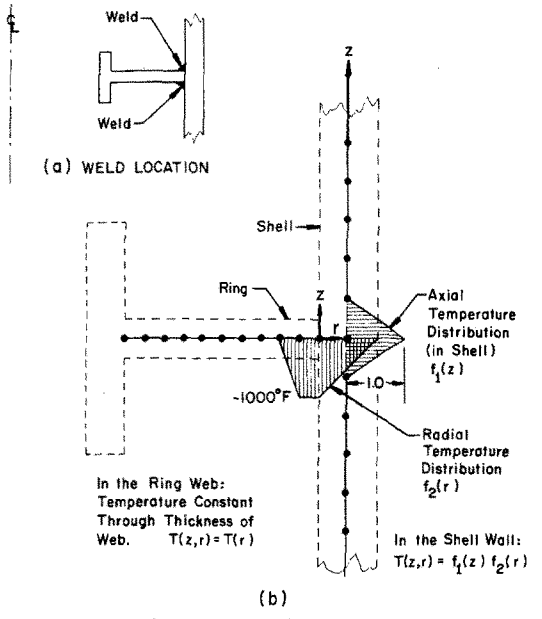

Fig. 19. Weld locations and simulation of weld thermal effect by local cooling.

deformations by treating the weld region as if it were cooled down below ambient temperature.

Figure 20 shows the prebuckling axisymmetrically deformed shape with increasing external pressure and a comparison with and without welding effects. The relatively advanced scalloping of the meridian corresponding to $p = 4100$ psi with the weld effect arises because of increased local plastic flow near the ring attachment points. The ring at the plane of symmetry moves inward rapidly with pressure increasing above 3500 psi because the flange yields and flows plastically, having zero tangent modulus for $P > 3500$ psi. (There is more welding required in the neighborhood of this ring than the others because the ring must first be welded to one of the halves of the shell and then the two halves of the shell must be welded together. Hence, in this area more of the material is cooled down by an amount approximately equal to the anneal temperature.)

Figure 21 shows predicted incipient buckling modes

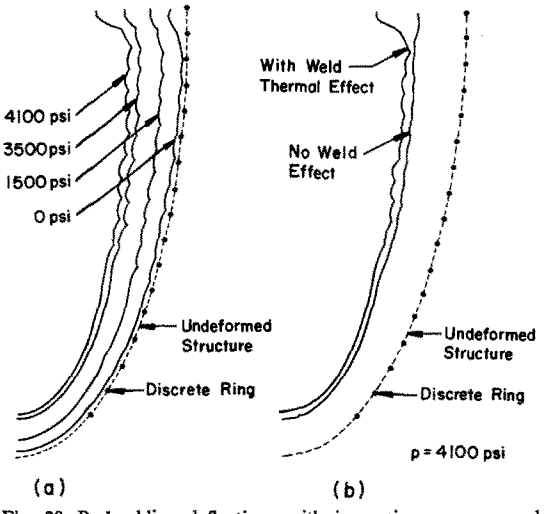

Fig. 20. Prebuckling deflections with increasing pressure and comparison with and without the weld cool-down effect.

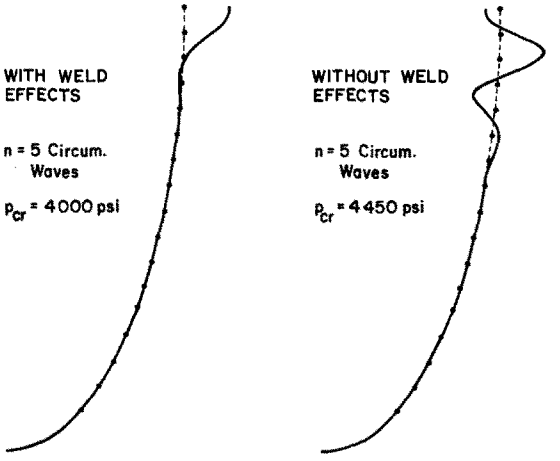

Fig. 21. Predicted bifurcation buckling modes and pressures with and without the weld cool-down effect included in the analysis.

with and without the weld thermal effect. The lowest predicted critical pressure corresponds in both cases to nonaxisymmetric buckling with 5 circumferential waves. The buckle modes are quite different in the two cases because of the increased amount of prebuckling plastic flow in the ring at the plane of symmetry predicted with the model which includes the weld effect.

3.6 *Creep effects*

3.6.1 *Test of the solution strategy-beam in bending.* The new strategy including primary creep[3] was tested with a simple example—a beam submitted to a constant bending moment sufficient to cause considerable plastic flow and creep at the external fibers. Some results are shown in Fig. 22. The lower part of the figure gives four curves corresponding to four different "major" time steps (see Section 1.1.5). For Δt = 1.0, 5.0 and 20.0 hr, the

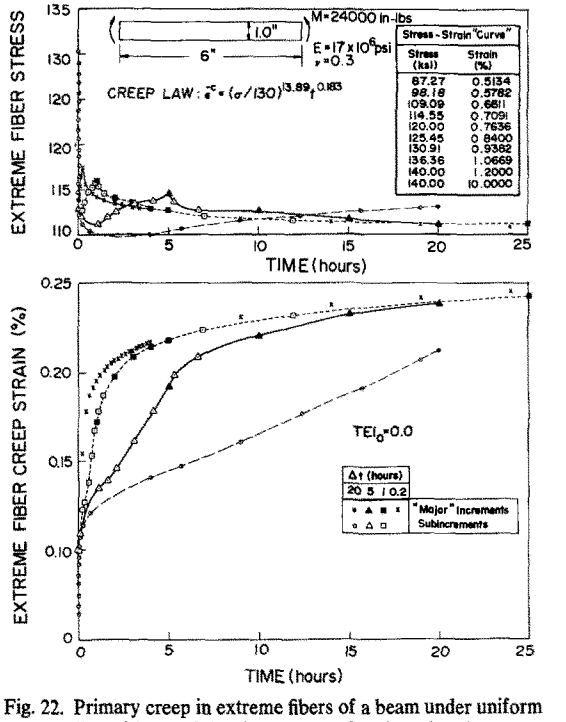

Fig. 22. Primary creep in extreme fibers of a beam under uniform bending with use of time increments of various durations.

creep strains for each subincrement are shown. The top part of the figure shows the history of extreme fiber stress. For times which are fairly large compared to the major time step, the predicted creep strains converge quite well with decreasing magnitude of major time increments. With large major time increments, the stress is overestimated at the ends of the increments, as seen especially from the curves marked with △ and ○ at the top of Fig. 22. This too-high stress leads to an overestimation of the creep rate during the ensuing time increment, a trend which continues to a diminishing degree until the predicted stresses and creep strains for all major time increments are reasonably close to one another. Thus, the error incurred in the early time increments due to the use of a large time increment is "washed out" as time progresses.

3.6.2. *Axisymmetric creep buckling of a cylinder.* Figure 23 shows deformations of an axially compressed thin cylinder. According to Samuelson[9] the three identical cylinders tested at a stress level of 12 kg/mm^2 buckled at 40, 44 and 57 min after application of the axial load. In the B0S0R5 model time steps of 0.025 hr were used. The temperature rise was applied at $t = 0$ and held constant for the duration of the case. The axial load was applied as shown in Fig. 23.

3.6.3 *Creep buckling of an externally pressurized ring-stiffened cylinder.* The configuration and locations of nodal points are shown in Fig. 24 and the stress–strain curve is given in Table 7. Symmetry conditions were applied at the symmetry plane. Figure 25 shows the loading schedule and gives the creep law. Solutions were obtained for each time indicated by a dot. Figure 26 gives load-deflection curves for computer runs in which the creep is neglected and included. If creep is neglected the predicted failure mode is nonaxisymmetric bifurcation buckling with 12 circumferential waves at a pressure of about 1810 psi. The prebuckling deflected shape (exaggerated) and the bifurcation buckling mode are shown in Fig. 27. With creep included the predicted failure mode is axisymmetric collapse at a pressure of

Table 7. Stress–strain curve used in the B0S0R5 analysis of the creep buckling of the ring-stiffened cylinder

STRESS (KSI)	STRAIN (%)
0	0
87.051	.484
93.580	.523
103.373	.599
109.902	.666
115.342	.759
119.500	.856
124.048	.999
132.753	1.332
136.017	1.665
139.282	1.998
139.282	10.000

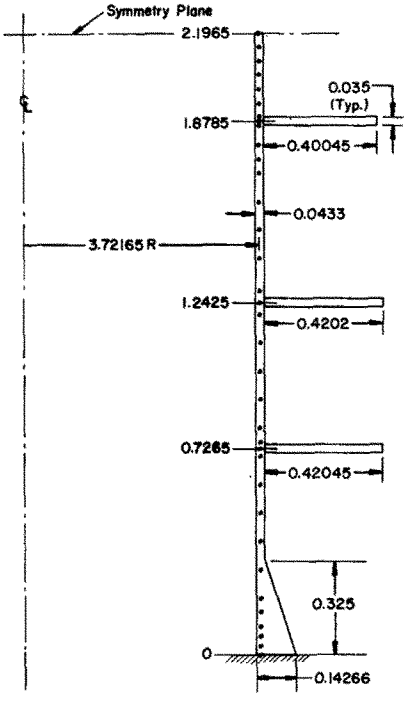

Fig. 24. Ring-stiffened cylinder under external hydrostatic pressure with nodal points used in the B0S0R5 analysis indicated.

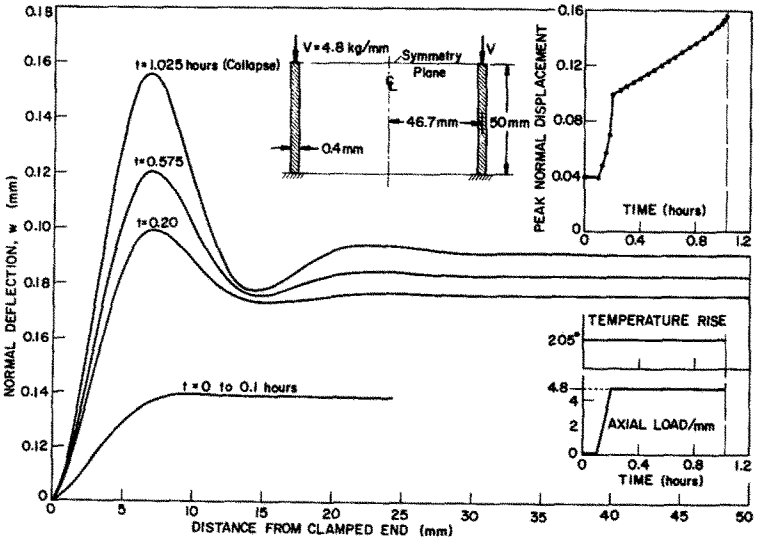

Fig. 23. Predicted axisymmetric creep buckling of an axially compressed thin cylinder tested by Samuelson.

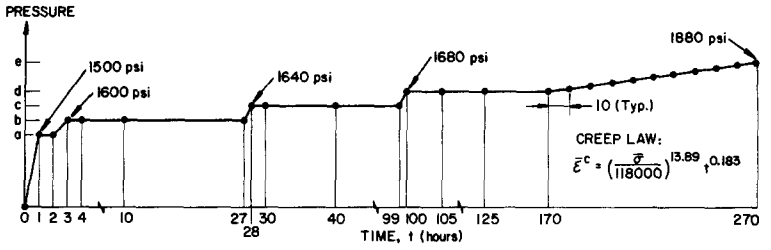

Fig. 25. Loading schedule for ring-stiffened cylinder.

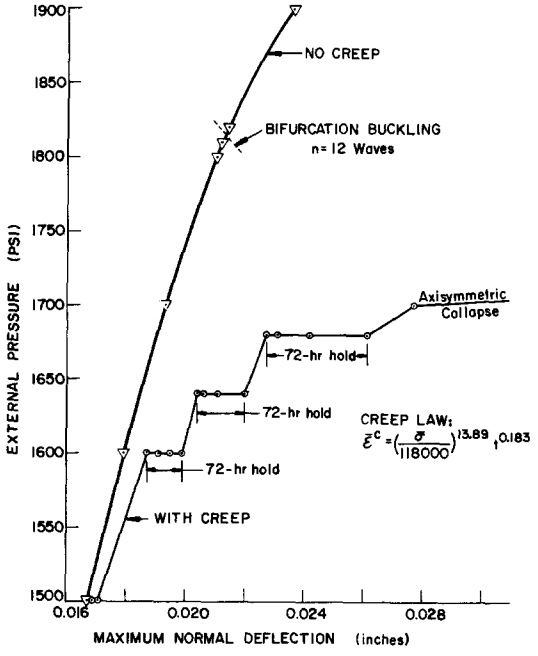

Fig. 26. Load-deflection curves for externally pressurized ring-stiffened cylinder predicted with and without primary creep included in the analysis.

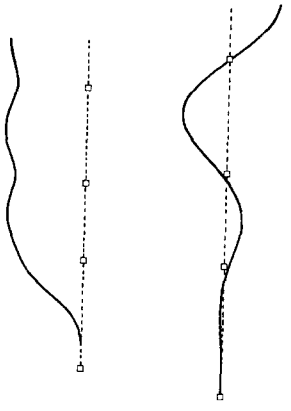

Fig. 27. Prebuckling deflected shape and bifurcation buckling mode for ring-stiffened cylinder with creep neglected in the analysis.

about 1700 psi. The growth of the axisymmetric buckle is shown in Fig. 28.

4. CONCONCLUSIONS

The theory on which the B0S0R5 computer program is based is briefly described and many numerical examples

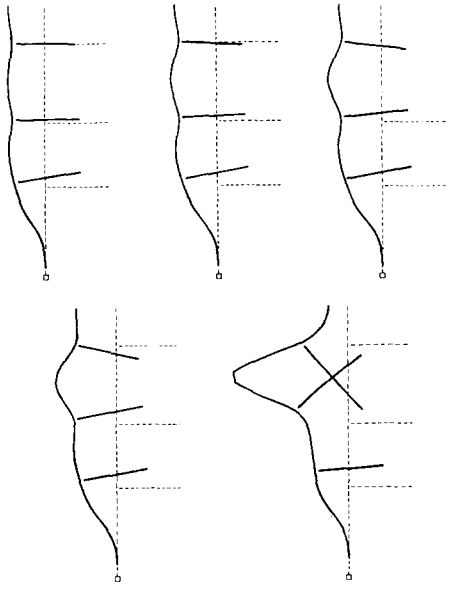

Fig. 28. Axisymmetric collapse of ring-stiffened cylinder with creep included in the analysis.

are given. This computer program runs on the CDC 6600 and UNIVAC 1108 or 1110 and is available from the developer. The documentation for BØSØR5 is[16].

REFERENCES

1. D. Bushnell, Large deflection elastic-plastic creep analysis of axisymmetric shells, *Numerical Solution of Nonlinear Structural Problems* (Edited by R. Hartung), Vol. AMD 6, p. 103 ASME, New York (1973).
2. D. Bushnell, Buckling of elastic-plastic shells of revolution with discrete elastic-plastic ring stiffeners. *Int. J. Solids Structures* **12**, 51–66 (1976).
3. D. Bushnell, A strategy for solution of problems involving large deflections, plasticity and creep. *Int. J. Num. Meth. in Engng* 1976, to be published.
4. D. Bushnell, Bifurcation buckling of shells of revolution including large deflections plasticity and creep. *Int. J. Solids Structures* **10**, 1287–1305 (1974).
5. F. R. Shanley, Inelastic column theory. *J. Aero. Sci.* **14**, 261 (1947).
6. J. W. Hutchinson, Plastic buckling. *Advances in Applied Mechanics*, (Edited by C. S. Yih), Vol. 14. Academic Press, New York (1974).
7. H. S. Levine, H. Armen Jr., R. Winter and A. Pifko, Nonlinear behavior of shells of revolution under cyclic loading. Grumman Research Department *Rep.* RE-426J (April 1972), Grumman Aerospace Corporation, Bethpage, New York. Also presented at National Symposium on Computerized Structural Analysis and Design, Washington, D.C., (27–29 Mar. 1972).
8. J. A. Stricklin, W. E. Haisler and W. A. von Riesemann,

Formulation, computation, and solution procedures for material and/or geometric nonlinear structural analysis by the finite element method, SC-CR-72 3102, July 1972, Sandia Laboratories, Albuquerque, New Merico.
9. L. A. Samuelson, Experimental investigation of creep buckling of circular cylindrical shells under axial compression and bending. *Trans. ASME J. Engng Indust.* 589–595 (Nov. 1968).
10. J. W. Hutchinson, On the postbuckling behavior of imperfection-sensitive structures in the plastic range. *J. Appl. Mech.* **39**, 155 (1972).
11. L. H. N. Lee, Inelastic buckling of initially imperfect cylindrical shells subject to axial compression. *J. Aero. Sci.* **29** 87 (Jan 1962).
12. S. C. Batterman, Plastic buckling of axially compressed cylindrical shells. *Am. Instit. Aeronaut. Astronaut. J.* **3**, 316 (Feb. 1965).
13. D. Bushnell and G. D. Galletly, Comparison of test and theory for nonsymmetric elastic-plastic buckling of shells of revolution. *Int. J. Solids Structures* **10**, 1271–1286 (1974).
14. See Ref. [2].
15. L. Boichot and T. E. Reynolds, Inelastic buckling tests of ring-stiffened cylinders under hydrostatic pressure. *David Taylor Model Basin Rep.* 1992, Washington, D.C. (May 1965).
16. D. Bushnell, B0S0R5—A computer program for buckling of elastic-plastic complex shells of revolution including large deflections and creep. *Vol. I: User's Manual, Input Data,* LMSC D407166; *Vol. II: User's Manual, Test Cases,* LMSC D407167; *Vol. III: Theory and Comparisons with Tests,* LMSC D407168. Lockheed Missiles & Space Co., Sunnyvale, Calif. (Dec. 1974).

APPENDIX

B0S0R5 OVERLAY STRUCTURE AND BRIEF DESCRIPTIONS OF SUBROUTINES

Purposes of the subroutines of the B0S0R5 preprocessor

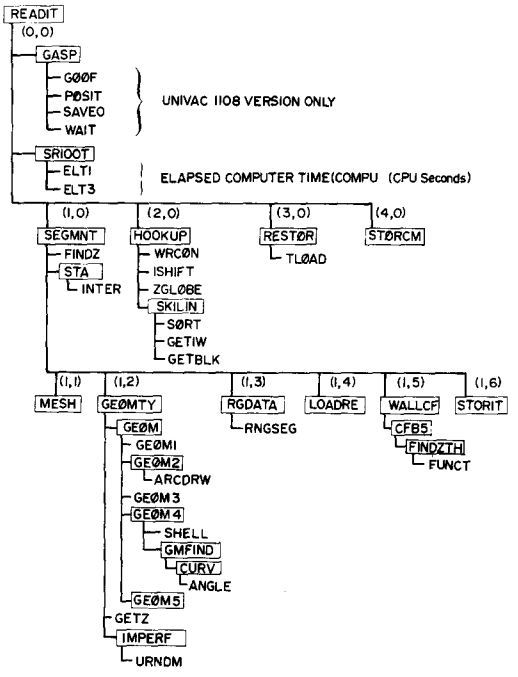

Fig. A1. B0S0R5 pre-processor overlay structure.

READIT The main program of the preprocessor. Calls the other subroutines.

GASP Transfers data to and from mass storage devices. There are two files involved: a large random-access file (called BLARGE on the control cards) and a small sequential-access file (called BSMALL and consisting of 550 words, most of these integers which identify where on BLARGE the random-access data blocks are stored).

SR100T Causes the elapsed CPU time from the beginning of the case to be printed.

SEGMNT Causes all input data for one shell segment to be read in and prepared for execution by the main processor.

FINDZ Linear interpolator.

STA Finds callout mesh point given various kinds of input data, such as axial stations, arc lengths to callouts, radii to callouts, etc.

MESH Reads in data for mesh point distribution and calculates lengths over which energy is "integrated" (lumped).

GEOMTY Reads in data for meridional geometry of a shell segment; imperfection; reference surface location relative to shell wall material.

GEOM Meridional geometry of reference surface.....

GEOM1 Flat plate, cylinder, cone

GEOM2 Spherical, ogival, toroidal.

GEOM3 Not used.

GEOM4 General meridional shape; ellipsoid; hyperboloid.

GEOM5 Not used.

GETZ Finds location of reference surface relative to shell wall "leftmost" surface.

IMPERF Reads in data for imperfection distribution along meridian.

RGDATA Reads in data pertinent to discrete ring stiffeners.

LOADRE Reads in data for temperature distribution, pressure and surface traction distribution, and line loads.
WALLCF Reads in data for wall construction and calculates elastic integrated constitutive law coefficients.
STORIT Stores data for a given shell segment temporarily on mass storage device.

HOOKUP Reads in data for time variation of loads, for juncture and other constraint conditions; calculates global axial coordinates for plotting purposes; and derives templates for the prebuckling and stability coefficient matrices.....
WRCON writes out the constraint conditions.
ISHIFT modifies constraint conditions to account for "extra" mesh points added at segment ends.
ZGLOBE calculates global axial coordinates of assembled structure.
SKILIN calculates the "skylines" of prebuckling matrices and stability matrices.

RESTOR Retrieves the data for each segment from mass storage and restores same data in bigger blocks to avoid too much I/O computer time in main processor runs.

STORCM Stores labeled common blocks for retrieval by main processor and post processor.

Purposes of the subroutines of the B0S0R5 main processor

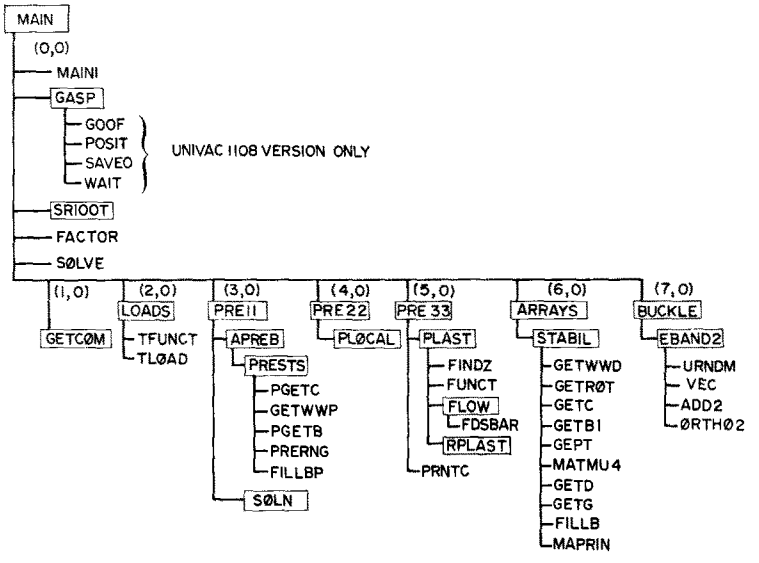

Fig. A2. B0S0R5 main-processor overlay structure.

MAIN The main program, calls the other subroutines.
MAIN1 A kind of "dummy" program for storing additional labeled common.
GASP For reading data to and from auxiliary storage devices. (See preprocessor)
SR100T Calculates and prints elapsed CPU time from start of case.
FACTR Decomposes a coefficient matrix into its lower triangular form. } Equation
SOLVE Performs back substitution for solution of equation system. } Solver
GETCOM Retrieves labeled common data stored on mass storage by STORCM. (See preprocessor)
LOADS Finds loads on the shell corresponding to the next time step.
PRE11 Sets up and solves the nonlinear (large deflection) prebuckling equations, given material properties.
APREB Sets up the equations for the next Newton iteration.
SOLN Factors and solves the system of linear equations derived by APREB
(loop over APREB and SOLN until Newton iterations converge.)
PRE22 Derives strains and stress resultants, given the solution obtained by PRE11.
PRE33 Finds updated material properties, given new values of total strains by PRE22.
PLAST retrieves temperature distribution and calculates new plastic and creep stain components in shell wall and in discrete rings....
FLOW uses flow or deformation theory to find plastic and creep strains components for a given point along the meridian and within the thickness of the shell wall (or within discrete ring).
RPLAST finds plastic and creep strains at several stations within each discrete ring.
PRNTC prints the integrated shell wall constitutive coefficients.
ARRAYS Derives the stability equations for given circumferential wavenumber, n, and calculates the stability determinant for a given time step.
STABIL calculates the stiffness matrix and the load-geometric matrix.
GETWWD finite-difference expressions for variable mesh.
GETROT derives 3×7 matrix relating rotations of shell wall to nodal point displacements.
CETC stores 6×6 matrix for local constitutive law.
GETB1 derives 6×7 matrix relating strains and curvature changes to nodal point displacements (kinematic law).
GETP derives pressure-rotation terms.
MATMU4 utility routine for finding $A = B^T C B$.
GETD derives 4×7 matrix relating shell wall displacements and meridional rotation to nodal point displacements.
GETG derives stiffness matrix for discrete ring; load-geometric matrix for discrete ring.
FILLB assembles local 7×7 matrices into global matrix.
MAPRIN not called by program in its present form. Prints out local matrices. A tool for debugging.

BUCKLE Eigenvalue solver for given circumferential wavenumber, n.
EBAND2 Uses inverse power iteration method to extract eigenvalues for stability problem.

Purposes of the subroutines of the B0S0R5 post processor

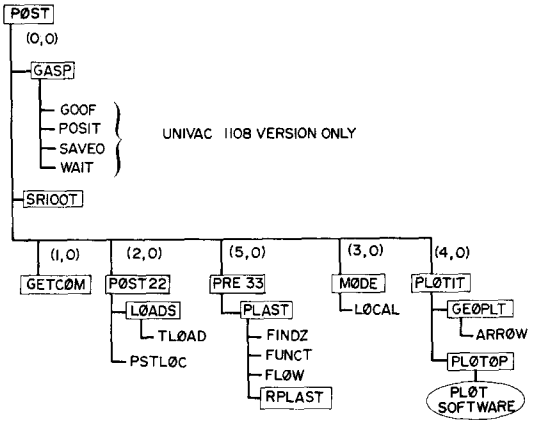

Fig. A3. B0S0R5 post-processor overlay structure.

POST The main program of the post processor, calls the other subroutines.
GASP Causes data to be transferred to and from auxiliary devices. (See preprocessor)
SR100T Not used.
GETCOM Retrieves labeled common data stored on mass storage by STORCM. (See preprocessor)
POST22 Calculates prebuckling displacements and stress resultants from solution vector corresponding to a given load or time step.
PRE33 Calculates plastic and creep strain components and prints these out for all meridional stations and integration points through the shell wall thickness.
PLAST, FLOW, RPLAST } see the definitions given in the section on the main processor.
MODE Calculates the buckling modal displacements from the eigenvector obtained by EBAND2 (see main processor).
PLOTIT Plots various information (presently only SC4020 plot software is available).
GEOPLT Undeformed and deformed prebuckling and buckling modal structures are plotted.
ARROW Affixes arrows showing direction of line loads and moments.
PLOTOP Plots displacements and stress resultants and modal displacements in x, y frames. Information for all shell segments plotted in series.